ORIGINAL RESEARCH

Single-Cell RNA Sequencing Provides New Insights into Therapeutic Roles of Thyroid Hormone in Idiopathic Pulmonary Fibrosis

Lan Wang[1,2*], Zhongzheng Li[1,2*], Ruyan Wan[1,2], Xin Pan[1,2], Bin Li[1,2], Huabin Zhao[1,2], Juntang Yang[1,2], Weiming Zhao[1,2], Shenghui Wang[1,2], Qiwen Wang[1,2], Peishuo Yan[1,2], Chi Ma[1,2,4], Hongmei Yuan[1,2], Mengxia Zhao[1,2], Ivan Rosas[3], Chen Ding[4], Baofa Sun[5], and Guoying Yu[1,2]

[1]State Key Laboratory of Cell Differentiation and Regulation, and [2]Henan International Joint Laboratory of Pulmonary Fibrosis, College of Life Science, Henan Normal University, Xinxiang, Henan, China; [3]Division of Pulmonary, Critical Care and Sleep Medicine, Baylor College of Medicine, Houston, Texas; [4]School of Life Sciences, Fudan University, Shanghai, China; and [5]College of Life Science, Nankai University, Tianjin, China

ORCID ID: 0000-0002-4124-1359 (G.Y.).

Abstract

Idiopathic pulmonary fibrosis (IPF) is a progressive fatal interstitial lung disease without an effective cure. Herein, we explore the role of 3,5,3′-triiodothyronine (T_3) administration on lung alveolar regeneration and fibrosis at the single-cell level. T_3 supplementation significantly altered the gene expression in fibrotic lung tissues. Immune cells were rapidly recruited into the lung after the injury; there were much more M2 macrophages than M1 macrophages in the lungs of bleomycin-treated mice; and M1 macrophages increased slightly, whereas M2 macrophages were significantly reduced after T_3 treatment. T_3 enhanced the resolution of pulmonary fibrosis by promoting the differentiation of *Krt8*$^+$ transitional alveolar type II epithelial cells into alveolar type I epithelial cells and inhibiting fibroblast activation and extracellular matrix production potentially by regulation of *Nr2f2*. In addition, T_3 regulated the crosstalk of macrophages with fibroblasts, and the *Pros1-Axl* signaling axis significantly facilitated the attenuation of fibrosis. The findings demonstrate that administration of a thyroid hormone promotes alveolar regeneration and resolves fibrosis mainly by regulation of the cellular state and cell-cell communication of alveolar epithelial cells, macrophages, and fibroblasts in mouse lungs in comprehensive ways.

Keywords: pulmonary fibrosis; T_3 therapy; single-cell RNA-seq; cell-cell communication; gene regulatory network

Pulmonary fibrosis (PF) is a progressive lung disease that is characterized by irreversible scarring of the distal lung, leading to respiratory failure and death (1). Currently, treatment of PF mainly relies on transplantation and short-term pharmacotherapy, which slow the rate at which forced vital capacity decreases; however, these treatments have limited clinical benefits (1). Many changes in cellular states and cell types occur after lung injury; for instance, stimulating the propagation of alveolar epithelial cells could increase the capacity of the lung to undergo self-repair, which is frequently limited by the surrounding microenvironment or niche (2, 3). The recruitment of monocytes results in changes in macrophage states and the conversion of fibroblasts to myofibroblasts during fibrogenesis (4). To date, several high-resolution reference maps of the human lung have been generated using single-cell sequencing, and these maps have revealed the molecular state of ~58 cell types in healthy and diseased lungs (5), the presence of aberrant cell populations that reside in the lungs in patients with idiopathic PF (IPF) (6), the heterogeneity of fibroblasts (7), and the presence of profibrotic macrophages in the lungs of humans and mice with PF (8, 9). These inherent or induced heterogeneities

(Received in original form March 3, 2023; accepted in final form June 29, 2023)

*These authors contributed equally to this work.

Supported in part by grant 2019YFE0119500 from the Ministry of Science and Technology, grant 202200382 from the Ministry of National Education, and grants 232102521025 and GZS2023008 from the Henan Province Science and Technology Project, People's Republic of China.

Author Contributions: G.Y. and B.S. designed the research work. L.W. and Z.L., performed the sample preparation, statistical analysis and manuscript preparation. H.Y., X.P., P.Y., M.Z., R.W., and B.L. performed experiments. H.Z., S.W., and C.M. contributed to the artwork. J.Y., W.Z., and Q.W. generated bleomycin-induced idiopathic pulmonary fibrosis and treatment with 3,5,3′-triiodothyronine in mice. I.R. and C.D. reviewed the manuscript.

Correspondence and requests for reprints should be addressed to Guoying Yu, Ph.D., Henan Normal University, 46 Jianshe Road, Xinxiang, Henan 453007, China. E-mail: guoyingyu@htu.edu.cn.

This article has a data supplement, which is accessible from this issue's table of contents at www.atsjournals.org.

Am J Respir Cell Mol Biol Vol 69, Iss 4, pp 456–469, October 2023

Originally Published in Press as DOI: 10.1165/rcmb.2023-0080OC on July 4, 2023
Internet address: www.atsjournals.org

and changes in cell types significantly contribute to pathological lung diseases; however, the cell-intrinsic properties that drive these processes and the strict spatiotemporal regulation of crosstalk among the various cell types that are activated or recruited after injury are not well understood, and little is known about how they respond to pharmacotherapy.

Single-cell RNA sequencing (scRNA-seq) technology has the potential to comprehensively elucidate the diversity of cell types and cell states as well as the molecular programs underlying these differences (10). scRNA-seq can provide detailed insights into the cellular architecture and the molecular mechanisms that drive lung regeneration and repair at the single-cell level, and scRNA-seq can be used to compare and characterize intercellular communication (11) and, thus, draw conclusions about single-cell regulatory networks (12, 13). scRNA-seq and the associated methods will facilitate the development of novel personalized therapeutic regimens for treating lung disease (10).

Our previous studies demonstrated that the administration of thyroid hormones attenuated mitochondria-regulated apoptosis in alveolar epithelial cells and restored mitochondrial function in bleomycin-treated mice (14); however, the roles of other cell types, changes in cellular states, and cellular interactions are currently unknown. Here, we integrated single-cell sequencing, bulk RNA sequencing (RNA-seq), and mass spectrometry to construct a multi-omics transcriptomic and proteomic atlas of healthy mouse lungs, mouse lungs with bleomycin-induced fibrosis (BLM), and mouse lungs treated with 3,5,3′-triiodothyronine (T_3). We performed a comprehensive analysis, and our findings increase the understanding of T_3 and the effects of thyroid hormones on epithelial transformation, fibroblast activation, and macrophage turnover. Overall, this work elucidates the mechanism by which T_3 therapy affects PF in mice at unprecedented resolution.

Some of the results of these studies have been previously reported in the form of an abstract (15).

Methods

Construction of Bleomycin-induced PF and Treatment with T_3 in Mice

The procedure was approved by the Henan Normal University Institutional Animal Care and Use Committee (HTU2019-02). The mice were randomly assigned to groups that received intratracheal administrations of either 1.5 U/kg bleomycin (Hanhui Pharma) or an equivalent volume (50 μl) of 0.9% saline. Aerosol administration of T_3 (Sigma) at 40 μg/kg daily started at Day 10 after bleomycin administration, and equivalent volumes of 0.9% saline were administered as control.

Preparation of Single-Cell Suspensions from Mouse Lung

Lung tissue was transferred to gentleMACS C Tubes (Miltenyi Biotec) containing 4.9 ml HEPES buffer with collagenase D solution and DNase I solution for samples. The cells were filtered and washed with HEPES buffer and were spun down at 300 × *g* for 10 min. After removal of the supernatants, the cells were resuspended with the desired volume of phosphate-buffered saline with EDTA and BSA.

scRNA-seq Data Analysis

The R package Seurat was used for quality control, analysis, and exploration of scRNA-seq data (16).

Pseudotime and Velocyto Analysis

Pseudotime analysis was performed on epithelial cells using the Monocle 2 (17) R package. Binary or Sequence Alignment files were converted to the loom files with counts divided into spliced, unspliced, and ambiguous. The Velocyto.R package was applied to estimate RNA velocity (18).

Cell Communication Analysis

We used CellChat with default parameters to explore ligand-receptor interactions (11). The average gene expression is zero if the percentage of cells expressing the gene in one group is less than 25%.

Transcription Factor Regulatory Network Analysis

We performed transcription factor regulatory network analysis using the SCENIC (12) workflow with default parameters.

Gene Expression Regulation Network Analysis

We used the R package bigSCale2 to construct the gene regulatory networks (GRNs) (13). Networks were constructed under the default parameter with an edge cutoff of 0.8 for the correlation coefficient. Networks were visualized using Cytoscopes software, Version 3.8.9 (19).

Raw Peptide Data Acquisition and Protein Quantification

Raw proteome data were processed using Firmiana (20). Proteome qualification was performed as previously reported with the iBAQ algorithm, followed by normalization to the fraction of total.

Bulk RNA-seq

The isolated RNA was then enriched for poly(A) templates and submitted for whole mRNA sequencing on the Illumina HiSeq 4000. Whole lung tissue bulk RNA next-generation sequencing reads were aligned to the mouse reference genome mm10 using STAR (21).

Fluorescence Microscopy and Analysis

For immunofluorescence, fixed lung tissues were incubated on glass coverslips with the primary antibodies overnight at 4°C in 3% BSA-PBS with 0.1% Triton X-100 (Solarbio) to permeabilize the cells, followed by incubation with the secondary antibodies (Affinity) for 1 hour at 37°C.

RNA Isolation and Quantitative PCR

RNA was isolated from samples using the RNeasy kit (Qiagen) as instructed. Furthermore, cDNA synthesis and quantitative PCR reactions were performed. Data were analyzed using R software to determine statistical significance ($P < 0.05$) by using Welch's *t* test.

Availability of Data and Material

The raw data have been deposited to the Sequence Read Archive Consortium (https://www.ncbi.nlm.nih.gov/sra) with the project ID PRJNA849722. All processed data needed to evaluate the conclusions in the paper are present here and in the data supplement.

Results

T_3 Supplementation Significantly Altered Gene Expression in Transcription and Translation in the Lungs of Bleomycin-treated Mice

To comprehensively understand the therapeutic role of T_3 in treating PF, RNA-seq, we performed mass spectrometry and scRNA-seq on the lungs of mice treated with a saline control (saline group), mice with BLM (BLM group), and mice treated with bleomycin plus T_3 (BLM+T_3 group) (Figure 1A). Micro–computed tomography imaging and

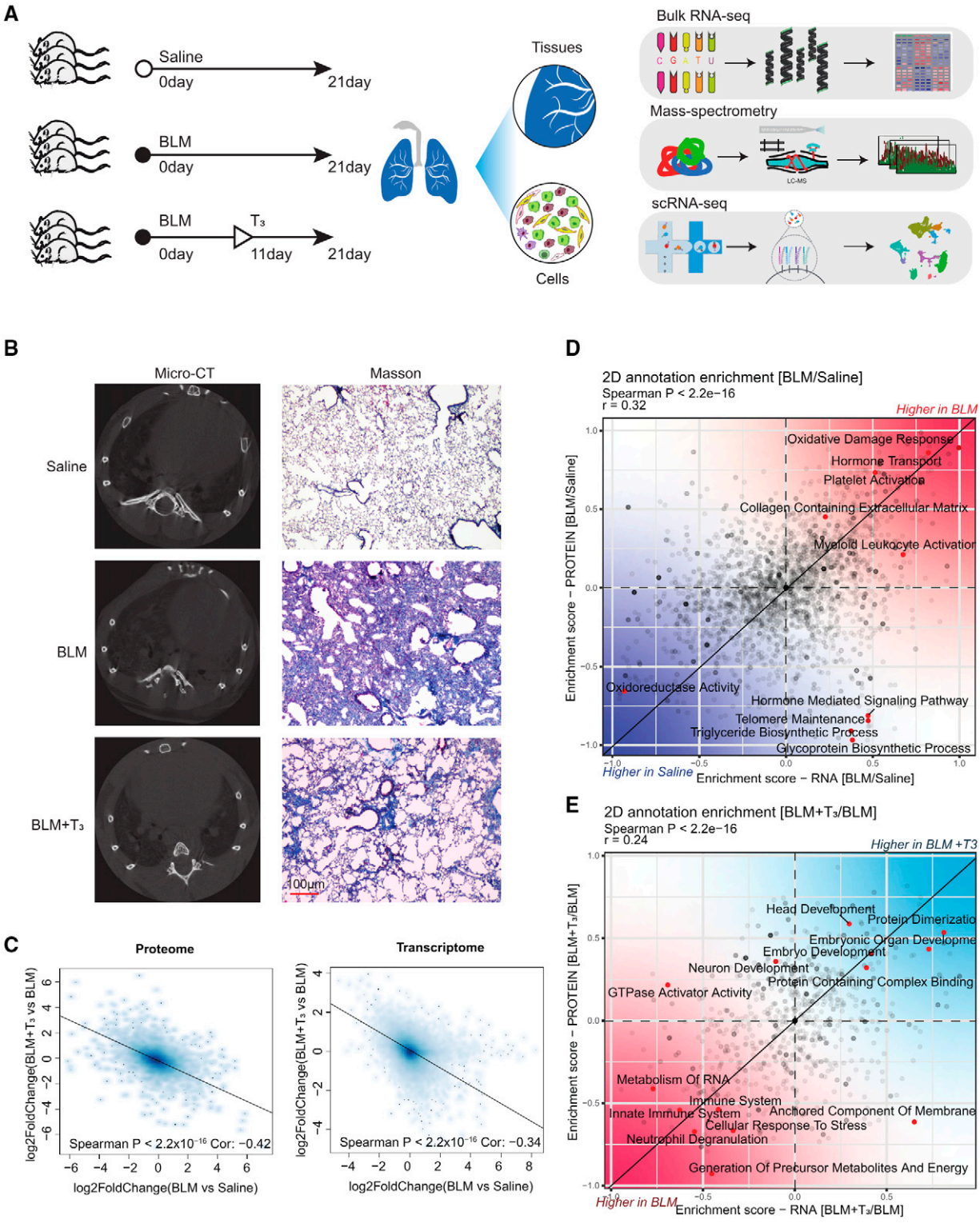

Figure 1. Integrative analysis of 3,5,3′-triiodothyronine (T_3) therapy for pulmonary fibrosis. (*A*) Information of bleomycin-induced pulmonary fibrosis and treatment with T_3 in mice. Schematic of the experimental process of the analysis of lung tissues from mice treated with saline control (saline group), mice with bleomycin-induced fibrosis (BLM group), and mice treated with bleomycin plus T_3 (BLM+T_3 group) by bulk RNA sequencing (RNA-seq), single-cell RNA-seq (scRNA-seq), and experimental verification (Mass spectrometry). (*B*) Left: representative micro–computed tomography images of lung tissues. Right: collagen deposition was detected by Masson staining. More collagen deposition/fibrosis in the pulmonary parenchyma was found in the BLM-treated mice. Compared with the BLM group, collagen deposition in the BLM+T_3 group was significantly reduced (shown at right). Scale bar, 100 μm. (*C*) Spearman's correlation analysis of the expression level

Masson staining revealed the positive therapeutic effect of T_3 (Figure 1B). Analysis of the RNA-seq datasets (*see* Table E1 in the data supplement) revealed that the $\log_2$ fold change of all genes between the BLM group and the saline group is negatively correlated with that between the BLM+T_3 group and BLM group (Figure 1C), indicating that bleomycin-induced gene expression alterations could be rescued by T_3 administration, and the proteomic results were consistent with the RNA-seq results (Figure 1C; *see* Table E2). Furthermore, we performed a two-dimensional annotation enrichment analysis using differentially expressed genes (DEGs; $P < 0.05$; Table E1) and differentially expressed proteins ($P < 0.05$; Table E2) between the BLM group and the saline group to reveal common or distinct regulation of gene annotation categories in the transcriptome or proteome. Most genes of the two-dimensional annotation enrichment scores showed a significant positive correlation between the transcription and translation levels (Spearman's $P < 2.2 \times 10^{-16}$); these genes were involved in the disorder of mitochondrial function, extracellular matrix (ECM) deposition, platelet activation, and myeloid leukocyte activation (Figure 1D). It is interesting that, on BLM treatment, the increased enrichment scores of hormone transport were observed in both the transcriptome and proteome datasets, but the enrichment score of the hormone-mediated signaling pathway only was increased at the RNA level; conversely, those of the telomere maintenance and metabolic processes were increased at the RNA level but decreased at the protein level (Figure 1D). After T_3 treatment, several hallmarks of regeneration and immunity, including a decline in immune function and upregulation of prodevelopment pathways revealed a significant positive correlation between the transcription and translation levels (Figure 1E).

Single-Cell Atlas of Lungs from T_3-treated Mice with BLM

We observed a good correlation between the real and *in silico* bulk data, thus excluding strong biases by the single-cell isolation procedures (*see* Figure E1A). After quality control and cluster annotation (Figures E1B and E1C), uniform manifold approximation and projection was used to visualize clusters of 31,385 single cells (Figure 2A). We then generated subsets of the whole lung datasets, which were classified into four major cell types: *Epcam*+ epithelial cells, *Pecam1*+ endothelial cells, *Col1a2*+ stromal cells, and *Ptprc*+ immune cells (Figure E1D). From these subsets, we derived cluster identities that were manually annotated using previously established single-cell signatures of the mouse lung (22). The final annotation identified 10 cell types, which were characterized by unique marker gene expression profiles (Figures 2B, 2C, and E1E; *see* Table E3). We observed changes in the cell proportions of different cell types. Previous findings have shown that the epithelial barrier in IPF is compromised (23) and that monocytes and macrophages are heavily infiltrated (24). The permutation-based statistical test (differential proportion analysis) (25) revealed that the epithelial cells had already been significantly contracted ($P < 2.2 \times 10^{-16}$), and the monocytes ($P = 0.004$) and macrophages ($P < 2.2 \times 10^{-16}$) had been significantly expanded (Figure 2D). In addition, a significantly decreased proportion of B cells ($P < 2.2 \times 10^{-16}$), neutrophils ($P < 2.2 \times 10^{-16}$), natural killer cells ($P < 2.2 \times 10^{-16}$), and T cells ($P = 0.043$) were observed in BLM-induced mice (Figure 2D; *see* Table E4). Angiogenesis and impairment of the epithelial barrier had recently been implicated in lung fibrosis homeostasis and pathogenesis for a long time (26). Notably, after T_3 administration, fibrotic mice exhibited dramatic changes in the relative proportion of cell lineages, which were characterized by significant reduction of endothelial cells ($P = 0.005$) and expansion of epithelial cells ($P = 0.009$) and neutrophils ($P = 0.002$) (Figure 2D; Table E4). Furthermore, we characterized the changes in molecular expression in response to T_3 treatment. In bleomycin-induced fibrotic mice, *Cdkn2b* exhibited high expression in epithelial cells, *Col1a2* showed high expression in fibroblasts, and *Cd74* displayed high expression in macrophages. However, treatment with T_3 significantly reduced the expression of these genes, leading to a tendency for them to return to the expression levels observed in saline group (Figure 2E).

Molecular Characterization of the Effects of T_3 Treatment on BLM in Mouse Lungs

A total of 658 fibrosis-related DEGs across 10 cell types were observed between mice with BLM and control mice, and most of them were prevalent in fibroblasts, alveolar epithelial cells, macrophages, and endothelial cells; therefore, we further investigated the effect of T_3 treatment on the expression of these fibrosis-related DEGs in three groups. By means of modularized analysis of the fibrosis-related DEGs, we deconvoluted changes in gene expression to various cell types and identified five efficient modules of upregulated fibrosis-related DEGs in mice with BLM (Figure 3A); these modules were generally related to immune reactions and ECM organization, including Module 1 (mainly attributed to macrophages) and Module 5 (mainly attributed to fibroblasts; Figures 3A and 3B). We also found that T_3 effectively inhibited the formation of the ECM but did not inhibit the degradation of the ECM by macrophages. Five modules of downregulated fibrosis-related DEGs were identified in mice with BLM, and these modules were associated with cell adhesion and epithelial cell function, including Modules 7, 8, and 11 (mainly attributed to immune cells) and Module 12 (mainly attributed to epithelial cells). Because most of the genes were hemoglobin, Modules 6 and 9 were excluded (Figures 3A and 3B). T_3 therapy notably restored these bleomycin-induced alterations in immune cells and epithelial cells and resulted in the significant recovery of parenchymal cells without causing excessive damage to the immune system.

To examine the transcriptional regulons underlying the pathogenesis of lung fibrosis

Figure 1. (*Continued*). changes of proteins (left) or genes (right) that were differentially expressed between the diseased and T_3-treated mouse lung. Linear fitting is indicated by a solid line. (*D*) The scatterplot shows the result of a two-dimensional annotation enrichment analysis based on fold changes between the BLM group and the saline group in the transcriptome (*x*-axis) and proteome (*y*-axis), which resulted in a significant positive correlation of both datasets. (*E*) The scatterplot shows the result of a two-dimensional annotation enrichment analysis based on fold changes between the BLM+T_3 group and the BLM group in the transcriptome (*x*-axis) and proteome (*y*-axis), which resulted in a significant positive correlation of both datasets.

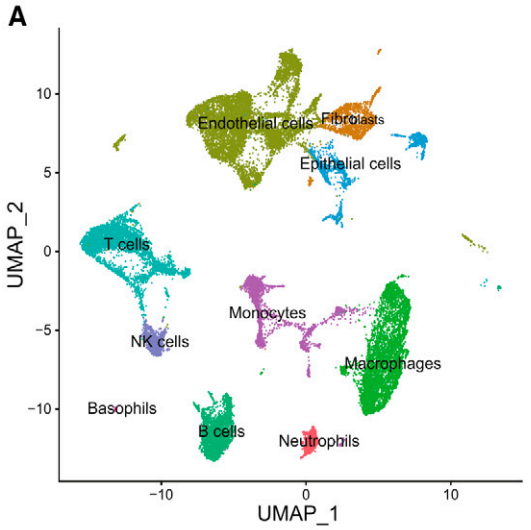

Cell type	Number of cells	Percentage
Endothelial cells	8058	31.56%
Macrophages	4602	18.02%
T cells	3727	14.60%
B cells	2241	8.78%
Monocytes	2183	8.55%
Fibroblasts	1579	6.18%
Epithelial cells	1359	5.32%
NK cells	943	3.69%
Neutrophils	763	2.98%
Basophils	71	0.28%

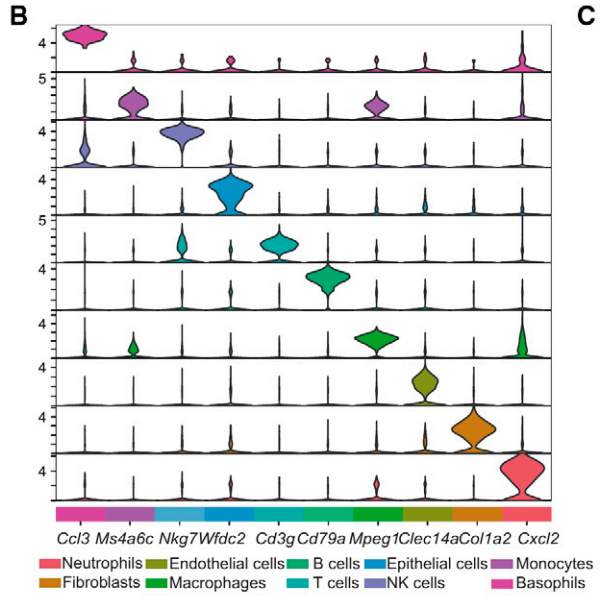

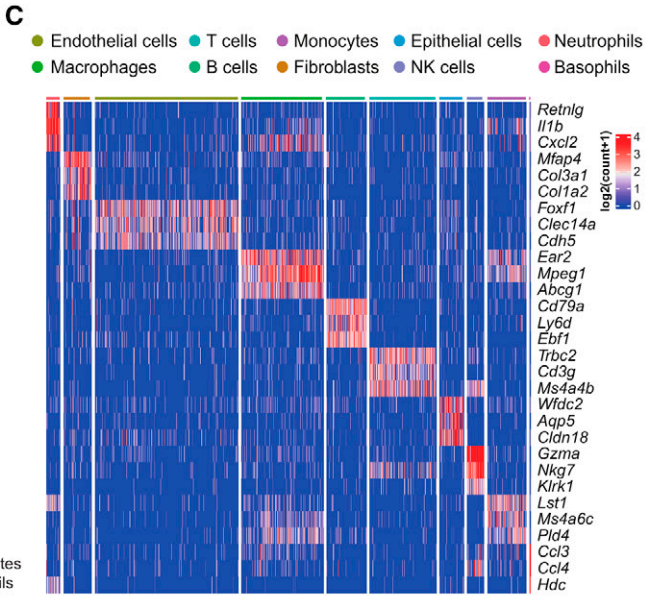

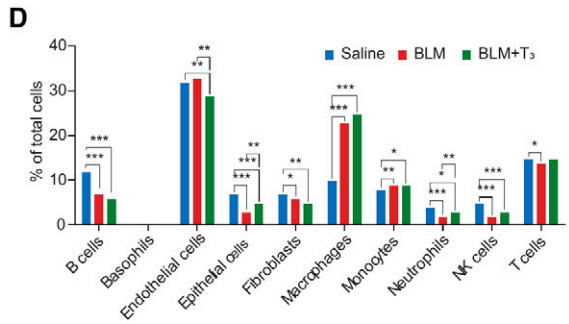

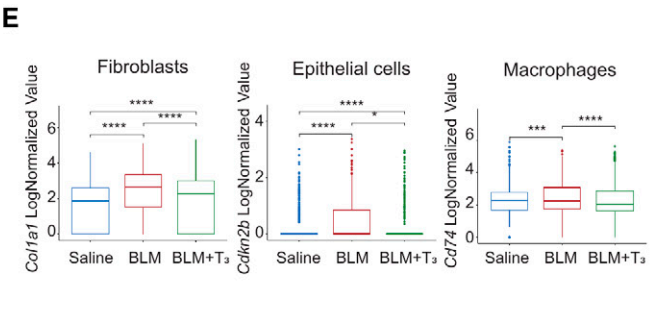

Figure 2. The single-cell RNA transcriptional atlases of the lungs of the control, BLM, and BLM+ T_3 groups by scRNA-seq. (*A*) Left: uniform manifold approximation and projection (UMAP) plot shows different cell types in scRNA-seq. Each point represents a single cell, colored according to cell types. Right: chart showing the number and percentage of each cell type. (*B*) Violin plots displaying the expression of canonical markers for each cell type. (*C*) Heatmap showing the gene expression signatures of the top three marker genes corresponding to each cell type in mouse lungs. Each column represents a cell type, and each row indicates the expression of one gene. Representative marker genes for each cell type are shown. (*D*) Bar plot displays the relative differential proportion of all cell types under treatment with saline, BLM, or BLM+T_3. (*E*) Box plot displays representative genes *Col1a1*, *Cdkn2b*, and *Cd74* in fibroblasts, epithelial cells, and macrophages, respectively, differentially expressed in saline, BLM, and BLM+T_3. NK = natural killer.

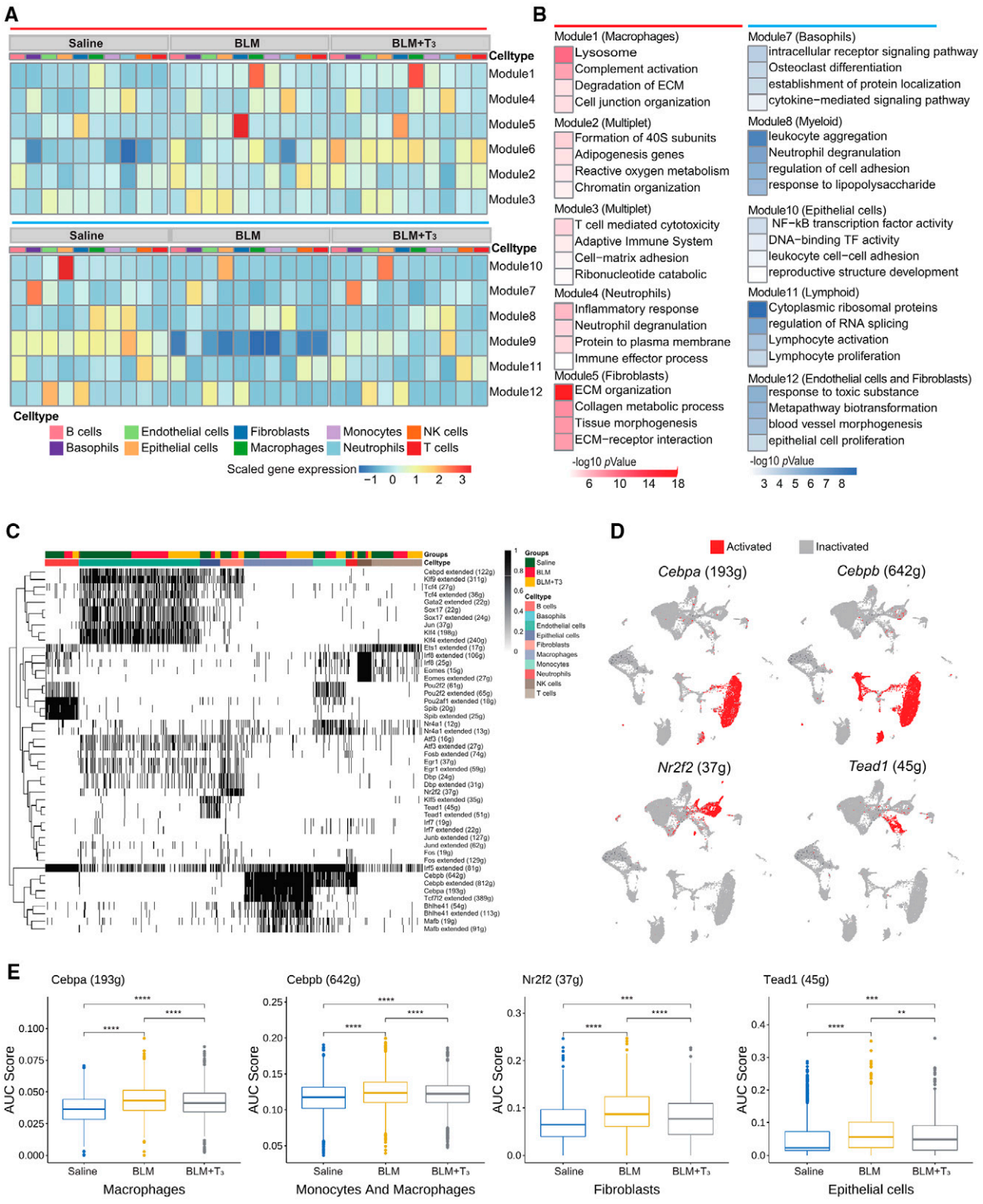

Figure 3. Transcriptional characteristics of the lungs of the BLM and BLM+ T_3 groups. (*A*) Heatmap shows fibrotic differentially expressed genes (DEGs), which were clustered into 12 modules by k-means analysis, across different cell types in the lungs of the BLM, BLM+T_3, and saline (control) groups. Top: Modules 1–6 indicate the specific upregulated modules in bleomycin-induced mouse lungs. Bottom: Modules 7–12 indicate the specific downregulated modules in bleomycin-induced mouse lungs. (*B*) Bar plot shows Gene Ontology term-enrichment analysis of fibrotic DEGs from different modules as shown in (*A*). Enrichment pathways of upregulated and downregulated DEGs are indicated in

and the mechanism underlying the therapeutic effects of T_3, we performed SCENIC analysis to identify candidate transcription factors that regulate gene expression across cell types (Figure 3C; *see* Table E5). Four regulons (*Cebpa*, *Cebpb*, *N2rf2*, and *Tead1*) were significantly activated in macrophages, fibroblasts, and epithelial cells (Figure 3D). We further quantified the area under the curve (AUC) value of each regulon in the three groups. As expected, the AUC values of the regulons in specifically activated cells were significantly altered in mice with BLM, and T_3 administration reversed these changes and restored the AUC values to their normal ranges (Figure 3E). Subsequently, we generated global, large-scale regulatory networks for all the cell types to assess the biological relevance of the differences between these networks using PageRank centralities and dynamical properties (*see* Table E6). Surprisingly, we found that *Tead1* and *Nr2f2* no longer had high PageRank in the regulatory networks from mice with BLM, whereas these factors consistently had the highest PageRank in the GRNs of fibrotic mice treated with T_3 and healthy control mice (*see* Figure E2A); these results indicate that *Tead1*- and *Nr2f2*-mediated regulation networks were disrupted in the lungs of bleomycin-treated mice, and T_3 therapy restored *Tead1* and *Nr2f2* to their crucial positions in the network, similar to observations in the control group. Together, these findings emphasize the contributions of T_3 to key processes related to molecular hemostasis in IPF.

T_3 Triggers the Immune System to Orchestrate the Microenvironment in PF

To elucidate the regulatory mechanisms by which immune cells are activated or recruited after injury, we extensively compared the changes in immune cells in the lungs of bleomycin- and T_3-treated mice (Figures 1D, 1E, 2D, and 3A–3D). On the basis of known markers and the ImmGen dataset (22), the myeloid cells were subclustered into 11 distinct cell subpopulations (Figures 4A; *see* Figures E3A and E3B). We reclustered segregated nucleus–containing atypical monocytes, which were characterized as Ceacam1+Msr1+Ly6C−F4/80−Mac1+ (Figure 4B), as identified in our data (Figure 4C) (27). It was consistent with the change of overall monocyte proportion that segregated nucleus–containing atypical monocytes were markedly increased in the fibrotic phase, but T_3 did not necessarily decrease its frequency (Figure 4D). Upregulated DEGs ($|\log \text{fold change}| > 0.25$; $P < 0.05$) between the BLM+T_3 group and the BLM group were mostly enriched in cell death and protection, immune response, development, and transport, whereas downregulated DEGs were mainly enriched in mitochondrial translation, Rap1 signaling, and Rho GTPase–related pathway (Figure E3C). These data suggest that profibrotic immune cells, especially monocytes and macrophages, are rapidly recruited into the lung after lung injury. Subsequent T_3 treatment did not affect the proportion of these immune cells, but it did alter gene expression pattern.

To further determine macrophage activation response to T_3 therapy, macrophages, including interstitial macrophages (IMs) and alveolar macrophages (AMs), as shown in Figure 4E, were divided into four clusters (Clusters 1–4) by unsupervised hierarchical clustering on the basis of lung-specific datasets (28, 29) (Figure 4E). Cluster 1 was identified as AMs, Cluster 2 was identified as monocyte-derived AMs, Cluster 3 contained cells with an intermediate phenotype between AMs and IMs, and Cluster 4 was defined as IMs. Clusters 2 and 3 were mainly present in the BLM and BLM+T_3 groups (Figure 4F), which suggests that they were activated and recruited to the microenvironment after bleomycin-induced lung injury. The M1 and M2 cell population of macrophages were evaluated and showed that there were many more M2 cells than M1 cells in Clusters 2 and 3 (Figure 4G) in bleomycin-treated lungs. The immunofluorescence staining for M1 and M2 cells in lung tissue sections from BLM+T_3-treated mice exhibited that M1 macrophages increased slightly, whereas M2 macrophages were significantly reduced (Figures 4H and 4I).

T_3 Suppresses Fibroblast Activation by Regulation of *Nr2f2* Activity

Fibroblasts are considered the central mediators of ECM production in PF (30, 31); therefore, we investigated the therapeutic effect of T_3 in fibroblasts. First, we attempted to score all fibrosis-related cells using a previously defined "fibroblast-activating gene set" (including 49 genes) to evaluate the potential profibrotic effect (32). The bleomycin-treated mice had a much higher fibrosis score than that of the healthy mice, and T_3 treatment significantly decreased the fibrosis score, indicating that T_3 could suppress the activation of fibroblasts (Figure 5A). To characterize fibroblasts, we first removed cells characterized as smooth muscle cells (*Des*, *Actg2*, and *Acta2*; *see* Figure E4A) or pericytes (*Pecam1*, *Cspg4*, *Nes*, and *Cox4i2*; Figure E4B). We further clustered fibroblasts into six subgroups on the basis of the expression pattern of highly variable features (Figures 5B and 5C); this strategy allowed us to identify myofibroblasts that consistently express type I and type IV collagen (Figures E4C and E4D). Four distinct fibroblast populations—including mitigatory myofibroblasts, oxidatively stressed fibroblasts, synthetically active fibroblasts, and inflammatory fibroblasts—were identified (Figures 5B and E4D). Synthetically active fibroblasts were mainly distributed in healthy lung, more oxidatively stressed fibroblasts were clustered into fibrotic lung tissues, and lesser inflammatory fibroblasts were found in fibrotic lung tissues (Figures 5C and 5D). Administration of T_3 significantly reduces the ratio of myofibroblasts and enhances the number of inflammatory fibroblasts (Figure 5D). In saline-treated mouse lung, fibroblasts often exist in a quiescent state; myofibroblasts were activated and present in higher levels in the fibrotic lung tissues, and they were significantly decreased in the lungs of T_3-treated mice (31, 33). Only 3% of fibroblasts from saline-treated lungs were assigned to the myofibroblast-like subcluster, compared with 61% of fibroblasts from

Figure 3. (*Continued*). red and blue, respectively. (*C*) Heatmap of cells and regulon binary scores with hierarchical clustering in 10 cell types under treatment with saline, BLM, or BLM+T_3. Black indicates active, and white indicates inactive, as inferred by SCENIC. (*D*) UMAP plot of major activated regions of transcription factors *Cebpa*, *Cebpb*, *Nr2f2*, and *Tead1*. (*E*) Box plot displays the changes of area under the curve (AUC) scores for *Cebpa*, *Cebpb*, *Nr2f2*, and *Tead1* regulons under saline, BLM, and BLM+T_3 treatment for mouse lungs. ECM = extracellular matrix; TF = transcription factor.

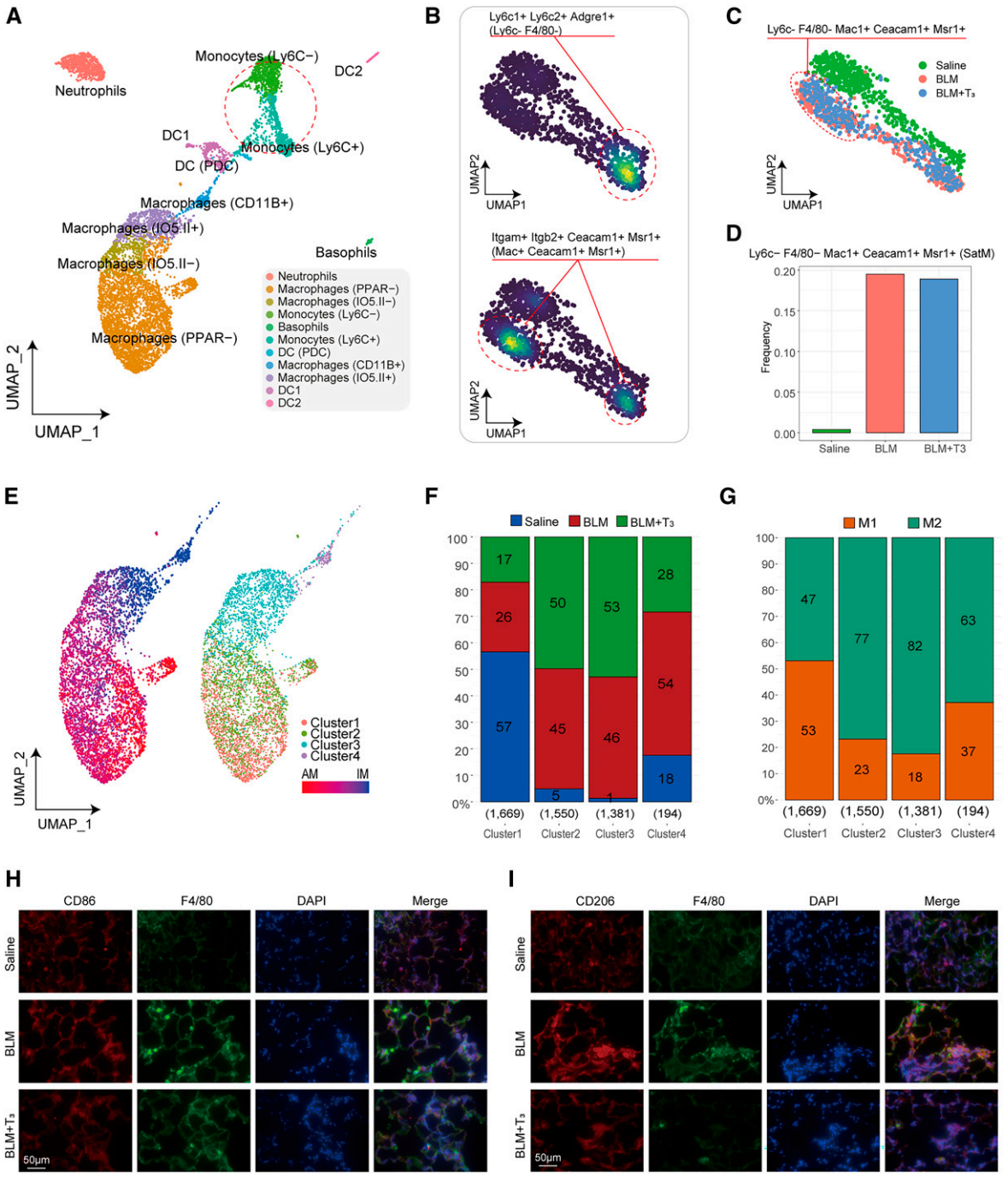

Figure 4. T_3 orchestrates the macrophage microenvironment in pulmonary fibrosis. (*A*) UMAP plot of 11 myeloid cell subsets (monocytes are indicated by the dotted line). (*B*) Nebulosa plots showing joint density of *Ly6c1*, *Ly6c2*, and *Adgre1*, or joint density of *Itgam*, *Itgb2*, *Ceacam1*, and *Msr1*, allowing precise identification of segregated nucleus–containing atypical monocytes (SatMs). (*C*) UMAP plot identifying clusters assigned to the saline group, BLM group, and BLM+T_3 group. (*D*) Bar plot shows that significant increases in cell number were observed in the *Ly6c−F4/80−Mac1+Ceacam1+Msr1+* SatMs in the BLM group compared with the saline group. No significant change in the cell number of SatMs was observed in the BLM+T_3 group compared with the BLM group. (*E*) Left: UMAP plot of the distribution feature of interstitial macrophages (IM) and alveolar macrophages (AM) under the total of macrophages. Right: UMAP plot of clusters 1–4 under the total of macrophages. The color code illustrates the cluster type identified. (*F*) The percent stacked bar plot shows the relative proportion of cells with saline, BLM, and BLM+T_3 treatment in clusters 1–4. (*G*) The percent stacked bar plot shows the differential populations of M1 and M2 macrophages in clusters 1–4. (*H*) Representative immunofluorescence staining of fibrosis tissues from BLM-induced mice. Tissue was stained for *F4/80* (green) and *CD86* (red). Nuclear counterstaining was conducted with DAPI (blue). Scale bar, 50 μm. (*I*) Representative immunofluorescence staining of fibrosis tissues from BLM-induced mice. Tissue was stained for *F4/80* (green) and *CD206* (red). Nuclear counterstaining was conducted with DAPI (blue). Scale bar, 50 μm.

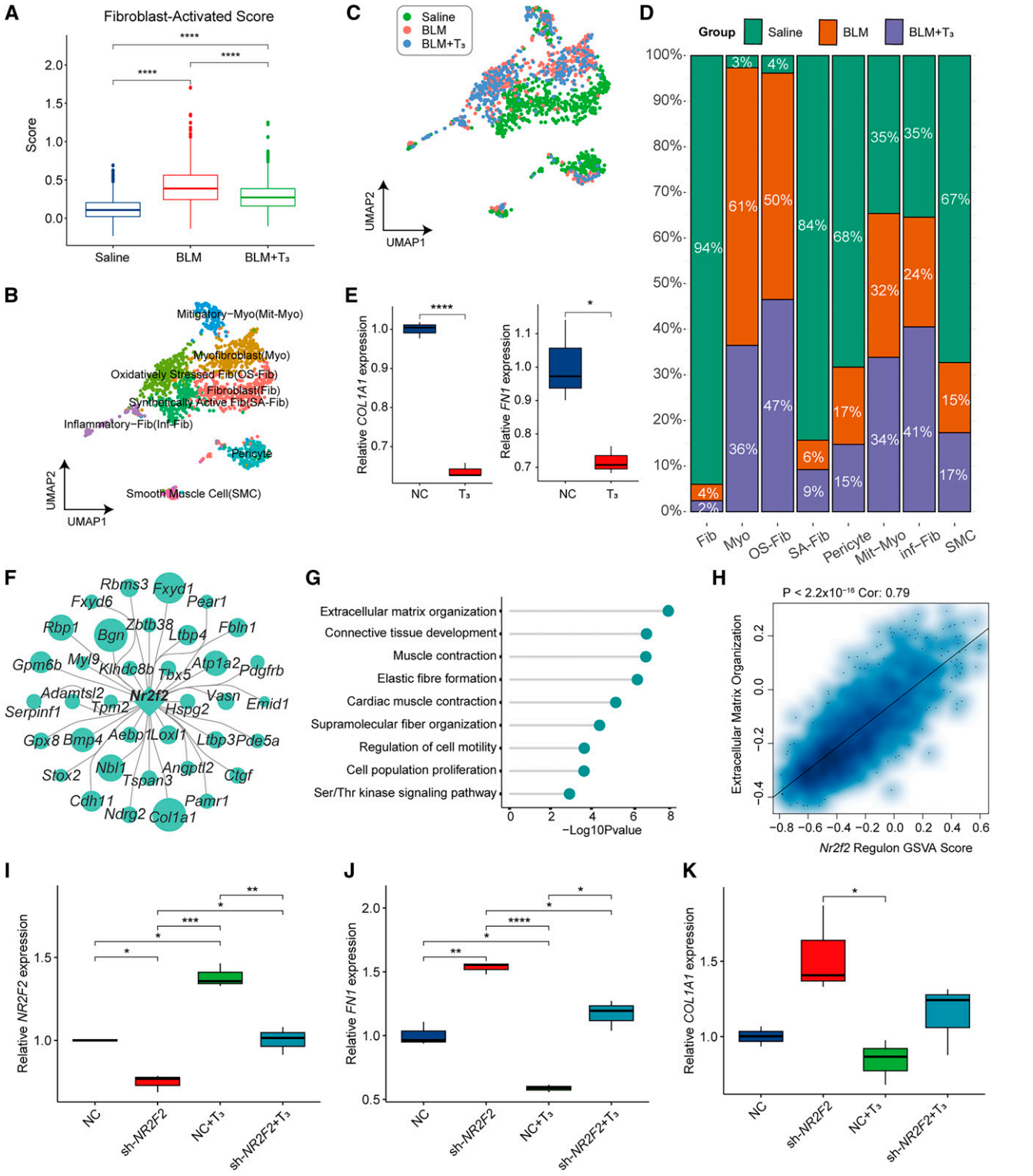

Figure 5. T_3 moderated the activation in fibroblasts. (*A*) Box plot shows the fibroblast alteration by fibrosis-activated scores under the treatment of saline, BLM, and BLM+T_3. (*B*) UMAP plot of the eight subgroups after clustering. (*C*) UMAP plot of fibroblasts with saline, BLM, and BLM+T_3 treatment. (*D*) The relative proportion of cells with saline, BLM, and BLM+T_3 treatment in eight subgroups. (*E*) Box plot shows quantitative PCR result of *COL1A1* and *FN1*. (*F*) Network plot shows that the downstream genes were regulated by *Nr2f2*. (*G*) Lollipop plot displays Gene Ontology term-enrichment analysis of *Nr2f2* regulon (genes targeted by *Nr2f2*). (*H*) Scatterplot shows Spearman's correlation analysis of the *Nr2f2* regulon score and gene set variation analysis (GSVA) score in ECM organization. Linear fitting is indicated by a solid line. (*I*) Box plot

bleomycin-treated lungs and 36% of fibroblasts from lungs treated with bleomycin and T_3 (Figure 5D). T_3 was validated to inhibit the expression of *FN1* and *COL1A1* level of TGF-β–induced transformation of MRC5 lung fibroblasts to myofibroblasts (Figure 5E).

In fibroblasts, the significantly activated regulons of *Nr2f2* regulated ECM production, lung development, and collagen biosynthesis (Figures 5F and 5G); the *Nr2f2* regulon was also positively associated with epithelial-mesenchymal transition and ECM organization, as demonstrated by gene set variation analysis (GSVA) (Figures 5H and E4E). We reasonably inferred that *Nr2f2* plays an important role in fibroblast activation and T_3 function. Although *NR2F2* expression decreased because of shRNA-mediated *NR2F2* silencing, T_3 administration still showed an effect of increasing *NR2F2* to some extent (Figure 5I). *NR2F2* silencing leads to increased *COL1A1* and *FN1* expression and significantly attenuates the effect of T_3 treatment (Figures 5J and 5K).

T_3 Promotes the Differentiation of Alveolar Type II Epithelial Cells (AT2) into Alveolar Type I Epithelial Cells (AT1)

Consistent with previous work, supplementation with T_3 inhibited PF by regulating mitochondrial homeostasis and function in epithelial cells (14) (*see* Figure E5A). To explore the effect of T_3 treatment on epithelial cells at a single-cell resolution, epithelial cells were clustered into seven distinct subtypes on the basis of known markers (Figures 6A and 6B). The main subgroups—including AT2, AT1, and *Krt8*+ transitional progenitor cells—were further identified using specific gene sets (Figure 6C). We performed pseudotime analysis of the progression of epithelial differentiation and transformation by Monocle 2 (17); the RNA velocity analysis also demonstrated that *Krt8*+ cells were prone to differentiate into AT1 in the saline group. This differentiation was impeded by bleomycin, and T_3 therapy restored it close to the normal level (Figure 6D). Immunostainings of *Krt8* in lung sections confirmed its continuous expression in fibrotic lung parenchyma. In contrast, the uninjured control lung and T_3-treated fibrotic lung showed *Krt8* transient expression *de novo* (Figure 6E).

The *Tead1* regulon is specifically activated in epithelial cells and regulated by T_3 (Figure 3D). *Tead1*-regulated genes and enriched signaling pathways were associated with epithelial morphogenesis (Figures 6F and 6G). We calculated the GSVA scores of the *Tead1* regulon and related pathways. A strong Pearson correlation coefficient ($R = 0.79$, $P < 2.2 \times 10^{-16}$) between the *Tead1* regulon score and pseudotime confirmed that *Tead1* was closely involved in epithelial morphogenesis (Figure 6H). As expected, T_3 inhibited the downstream pathway associated with PF regulated by *Tead1* (Figure E5B); however, we need more experiment details to support these findings in the future.

T_3 Coordinated the Homeostatic Crosstalk of Macrophages with Other Cell Types

Intercellular communications often drive cell heterogeneity and cell state transitions, and scRNA-seq data that provide gene expression information can be used to analyze and draw conclusions about cell-cell communication with CellChat (11). The cell communication analysis for all the cell populations was based on a ligand-receptor interaction database (11), and the incoming and outgoing signaling patterns (permutation test, $P < 0.05$) for the whole cell population were analyzed under disease and T_3 treatment conditions (*see* Figure E6A and Table E7). The results indicated that the total number and strength of inferred interactions were significantly increased in the BLM group, suggesting enhanced or abnormal intercellular communication under disease conditions, and T_3 therapy moderately decreased the number and strength of communication interactions (Figure E6B). Among the 10 cell types, the number and strength of interactions for both outgoing and incoming signals between macrophages and other cell types decreased significantly in the disease state, which indicates that immune surveillance was disrupted and that the immune response to lung injury was abnormal (Figures 7A and E6C). The number of interactions between epithelial cells themselves and between epithelial cells and endothelial cells or fibroblasts increased significantly (Figures 7A and E6C), which suggests that the epithelial barrier is actively repaired and affects the surrounding microenvironment; this may be the main cause of fibrosis. After T_3 therapy, the number and strength of the interactions between macrophages and other cell types increased significantly, which suggests the recovery of innate immunity and the reestablishment of immune surveillance (Figures 7A and E6C). We compared the relative flow of information through each signaling pathway to identify the active molecules that respond to T_3 therapy. The majority of signaling pathways involved in information flow—including B-cell activating factor (BAFF), macrophage migration inhibitory factor (MIF), protein S (PROS), growth arrest specific (GAS), colony stimulating factor (CSF), granulin (GRN), transforming growth factor beta (TGF-β), chemokine ligand (CCL), and angiopoietin-related protein (ANGPTL)—exhibited markedly increased levels under disease conditions, and T_3 therapy caused these levels to decrease, However, some other signaling pathways exhibited opposite changes, such as IL-1, FASLG, and PDGF, which were downregulated under disease conditions and upregulated after T_3 administration (Figures 7B and E6D).

Furthermore, we focused on more detailed cell-cell communication among fibroblasts, epithelial cells, and macrophages and performed subsequent ligand receptor analysis. In total, 63 ligand-receptor pairs (permutation test; $P < 0.05$)—including pairs in the TGF-β, PROS, SPP1 (secreted phosphoprotein), CCL, and MIF pathways,—were different among fibroblasts, epithelial cells, and macrophages (*see* Figure E7). Vascular endothelial growth factor signaling was observed exclusively in the epithelial cells of the lungs of saline-treated

Figure 5. (*Continued*). shows qPCR results of *NR2F2* in TGF-β–treated MRC5 fibroblasts injected with sh-NC, sh-*NR2F2* treated with DMSO, sh-NC treated with T_3, and sh-*NR2F2* treated with T_3. (*J*) Box plot shows qPCR result of *COL1A1* in TGF-β–treated MRC5 fibroblasts injected with sh-NC, sh-*NR2F2* treated with DMSO and T_3. (*K*) Box plot shows qPCR result of *FN1* in TGF-β–treated MRC5 fibroblasts injected with sh-NC, sh-*NR2F2* treated with DMSO, sh-NC treated with T_3, and sh-*NR2F2* treated with T_3. *$P < 0.05$, **$P = 0.05$–0.01, ***$P = 0.01$–0.001, and ****$P < 0.001$. Fib = fibroblasts; Inf-Fib = inflammatory fibroblasts; Mit-Myo = mitigatory myofibroblasts; Myo = myofibroblasts; NC = Negative Control; OS-Fib = oxidatively stressed fibroblasts; SA-Fib = synthetically active fibroblasts; sh = short hairpin RNA; SMC = smooth muscle cells.

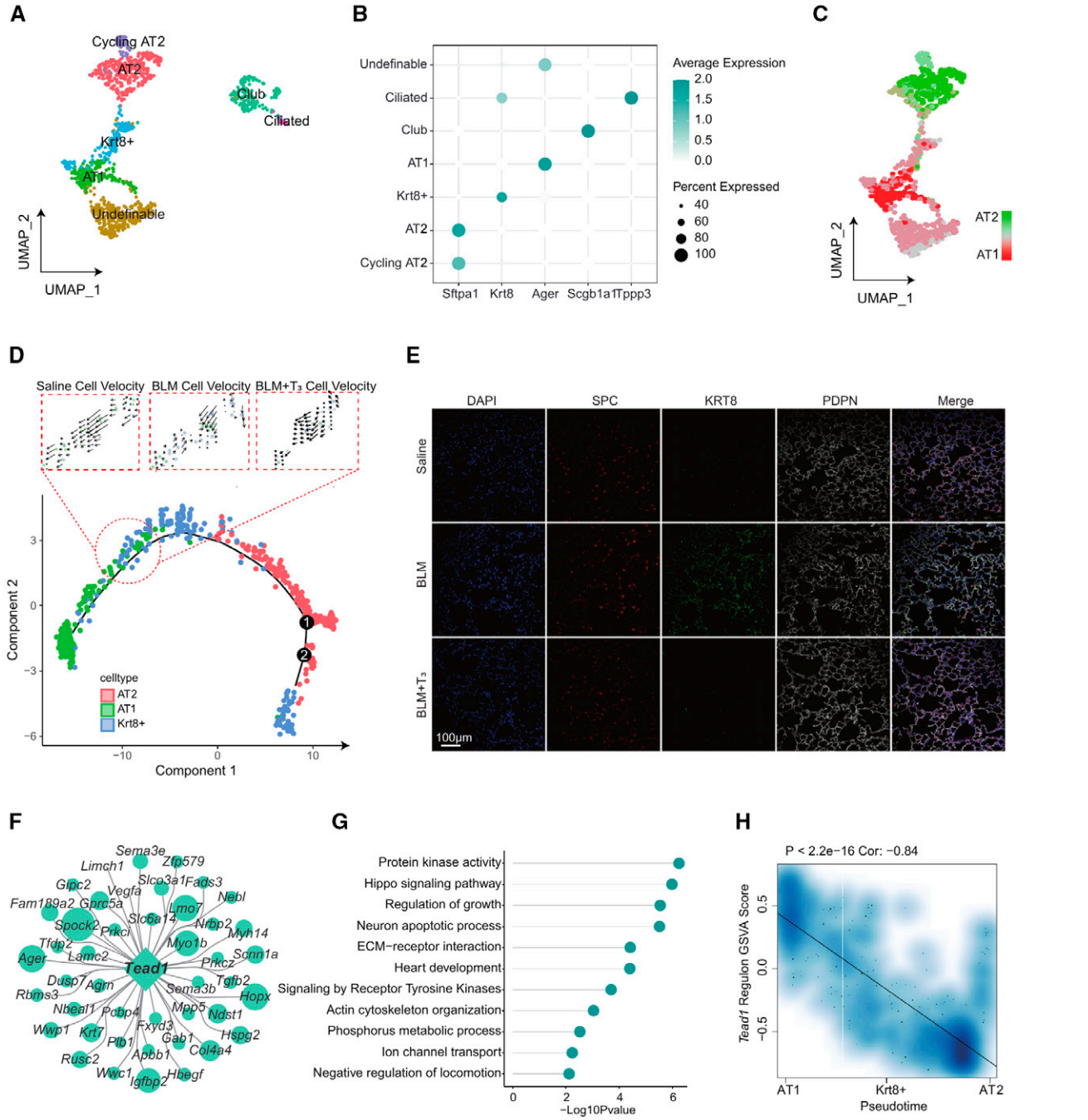

Figure 6. T_3 supplementation promotes epithelial cell differentiation and repair. (*A*) UMAP plot of the epithelial cells from the lungs of the saline, BLM, and BLM+T_3 groups by cell type, including AT2, AT1, club, *Krt8*$^+$ cells, cycling AT2, ciliated cells, and undefinable cells. (*B*) Bubble plot of the classical marker gene expression in the subsets of epithelial cells. (*C*) UMAP plots show the gene-set scores of alveolar type II epithelial cell (AT2)–related genes and alveolar type I epithelial cell (AT1)–related genes. (*D*) Velocity plot displays the DDR embedding colored by Louvain clusters with velocity information overlaid (arrows). (*E*) Immunofluorescence of *Krt8* on epithelial cells flushed from the lungs of the saline (top), BLM (middle), and BLM+T_3 (bottom) groups. Scale bar, 100 μm. (*F*) Network plot of *Tead1* regulon (genes targeted by *Tead1*). (*G*) Lollipop plot displays Gene Ontology term-enrichment analysis of *Tead1* regulon (genes targeted by *Tead1*). (*H*) Spearman's correlation analysis of the *Tead1* regulon score and pseudotime. Linear fitting is indicated by a solid line.

mice, and semaphorin signaling was observed exclusively between epithelial cells and macrophages under disease conditions (Figure E7).

We further studied the effect of macrophages on other cells and found that more specific pairs of ligands and receptors between macrophages and epithelial cells interacted in the BLM group. In particular, *Igf1* and *Igf1r* interacted only with the BLM group, and T_3 therapy completely eliminated this interaction. Between

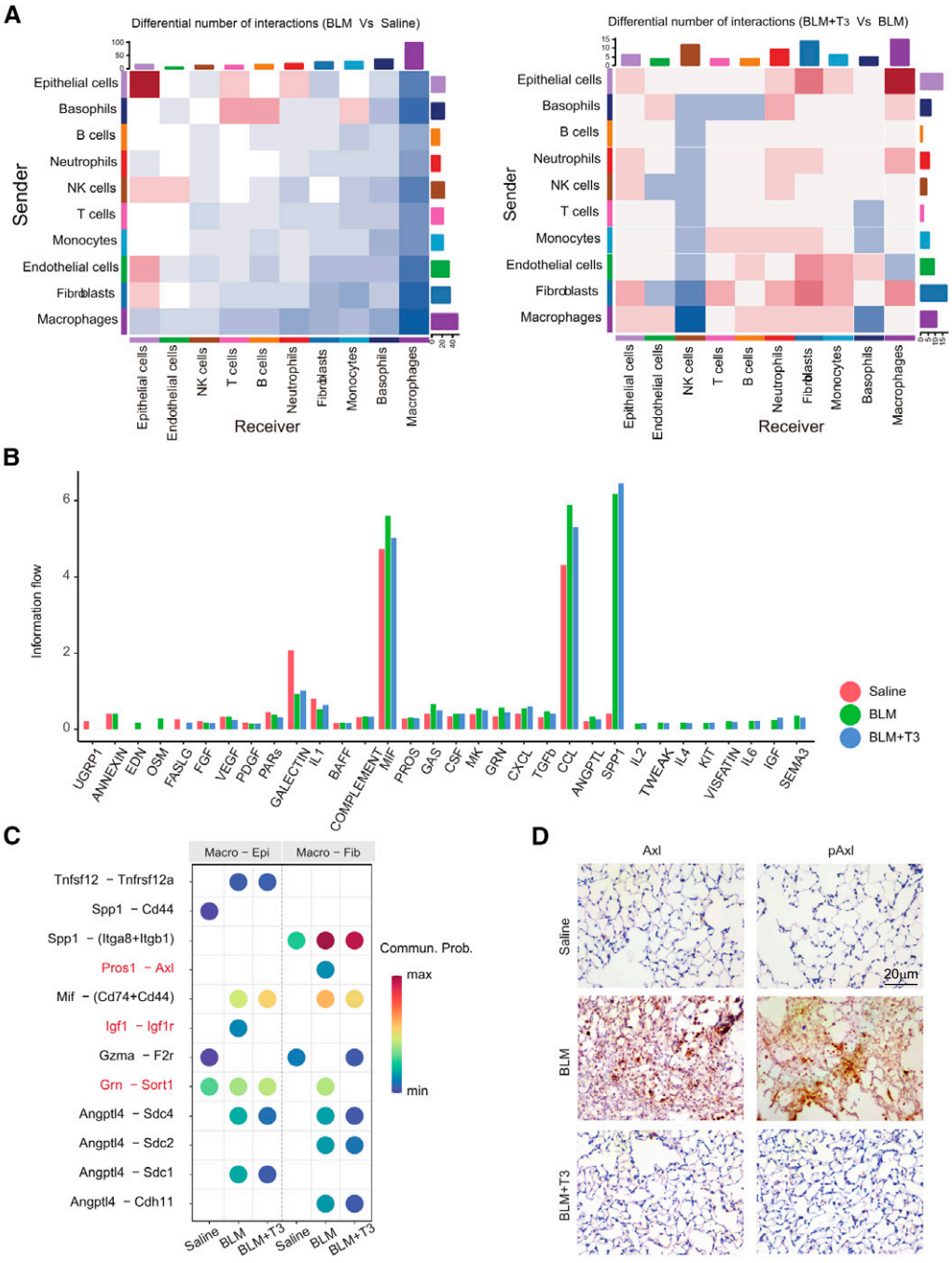

Figure 7. Cell-chat analysis of the communication between cells under saline, BLM, and BLM+T_3 treatment. (*A*) Heatmap of the differential interaction number in cells between the BLM and saline groups (left) and between the BLM+T_3 and BLM groups (right). (*B*) Bar plot shows the changes of ligand-receptor pair information flow among all cells under saline, BLM, and BLM+T_3 treatment. (*C*) Bubble plot shows the specific pair of ligands and receptors between macrophages and epithelial cells (Macro-Epi) and between macrophages and fibroblasts (Macro-Fib) under saline, BLM, and BLM+T_3 treatment. (*D*) Immunohistochemistry staining of Axl and pAxl in the lung tissue under saline, BLM, and BLM+T_3 treatment. Scale bar, 20 μm. Commun. Prob = Communication probability.

macrophages and fibroblasts, the communication of *Pros1-Axl* and Grn-Sort1 was mainly activated under the disease state, and T_3 therapy abolished this communication (Figures 7C and E7).

Elevated expression of *Axl* and pAxl in lungs with BLM was confirmed (Figure 7D); this upregulation of *Axl* was reversed by T_3 treatment. Immunohistochemistry analysis demonstrated that *Axl* and *pAxl* abundance in the lungs of bleomycin-treated mice was significantly inhibited by T_3 treatment (Figure 7D). These findings suggested that the elevation of *Axl* abundance in fibroblasts may be one potential target of T_3.

Discussion

scRNA-seq approaches make it possible to explore cell diversity at the single-cell level under healthy and disease conditions and provide insights into pathogenesis, mechanisms, and treatment (10). The emerging integration of multi-omics technologies provides opportunities to elucidate the cellular and molecular mechanisms underlying lung alveolar regeneration and fibrosis at cutting-edge resolution, which, in turn, allows the use of precision medicine in the treatment of fibrotic disease (34). To date, there are ~40 known cell types in the lung (10), but how to identify cell-specific and disease-specific changes in gene expression and how multicellular interactions respond to drug treatment in lung fibrosis remain unclear. Currently, some findings are available in the IPF Cell Atlas (35), including data about epithelial cell heterogeneity, profibrotic macrophages, and the subtypes of fibroblasts and myofibroblasts in fibrotic lungs; however, there is still a lack of detailed information about the cell-specific molecular changes that occur after treatment in patients with IPF or fibrotic animal models (30). In the present study, we built a single-cell atlas of lungs with BLM and BLM+T_3 to explore the mechanism by T_3 therapy in mice; we studied distinct cell types, cell-to-cell crosstalk, intercellular communication, and signaling networks, and we hoped to reveal novel potential targets for the cure of this disease.

Mesenchymal cells are the key source of pathological ECM deposition (33). Fibroblasts are recognized as the central mediator of ECM production in PF, which ultimately leads to architectural disruption and diminishes lung function (31, 36). We observed a significant change in the size of the fibroblast population in the lungs of bleomycin-treated mice, and the differentiation of fibroblasts to myofibroblasts was significantly altered after T_3 administration. Consequently, T_3 therapy markedly decreases fibrosis mainly by inhibiting fibroblast activation and reducing ECM deposition.

One primary feature of PF is alveolar epithelial cell injury and abnormal repair (37). Our previous study suggested that repeated injuries to epithelial cells drove lung fibrosis and that administration of T_3 enhanced the resolution of fibrosis and restored mitochondrial bioenergetics in murine lung epithelial cells (14). Evidence from the omics data analysis revealed that epithelial cell injury was repaired and integrity was restored after T_3 treatment. In PF, there is an ineffective transition from AT2 to AT1, which is characterized by the persistence of a transitional state marked by high expression of *Krt8* (23, 38). T_3 administration effectively promoted epithelial transformation by regulating the differentiation of *Krt8*+ cells; this discovery offers potential inspiration for therapeutic interventions that aim to modulate the plasticity of AT2 cells in PF. Further detailed mechanisms need to be studied in the future.

The promotion of fibroblast activation by prolonged or recurrent epithelial injury is regulated by macrophages in PF (39), and under pathological conditions, bleomycin treatment recruits monocytes and promotes their differentiation into more macrophages during inflammation resolution (40), subsequently activating more macrophages to regulate the fibrotic microenvironment (28, 41). T_3 treatment enhanced the intercellular interactions between macrophages and fibroblasts. *Pros1-Axl* ligand-receptor pairs exhibited different responses to T_3 in macrophages and fibroblasts. The activation of *Axl* could promote fibrotic phenotypes in fibroblasts (42, 43) and repair epithelial cell damage (44, 45), and T_3 therapy inhibited *Axl* expression in fibroblasts and activated *Axl* signaling in epithelial cells. These findings suggested that T_3 played different roles in different cell types and signaling networks.

Although this study resulted in prominent findings, there are some limitations that should be mentioned. First, ligand-receptor pair analysis is an excellent tool for the prediction of biological processes, but verification of ligand-receptor pair functions and transcription factor target genes is a challenging task *in vitro* and *in vivo*. Second, examining the differences in biological processes, mechanisms, and inherent limitations of lineage-tracing studies between human patients with IPF and the bleomycin-induced mouse model may still be a great challenge (10).

The high-resolution overview of the antifibrotic effect of T_3 on cell types, cell states, and gene expression reprogramming and communication highlights different mechanisms and provides new insights on the pathogenesis and treatment of lung injury and fibrosis. This study indicates that the use of thyroid hormones may be a potential therapeutic strategy for treating acute lung injury and PF. ■

Author disclosures are available with the text of this article at www.atsjournals.org.

References

1. Lederer DJ, Martinez FJ. Idiopathic pulmonary fibrosis. *N Engl J Med* 2018;378:1811–1823.
2. Raghu G, Remy-Jardin M, Myers JL, Richeldi L, Ryerson CJ, Lederer DJ, *et al.*; American Thoracic Society, European Respiratory Society, Japanese Respiratory Society, and Latin American Thoracic Society. Diagnosis of idiopathic pulmonary fibrosis. An official ATS/ERS/JRS/ALAT clinical practice guideline. *Am J Respir Crit Care Med* 2018;198: e44–e68.
3. McDonald LT. Healing after COVID-19: are survivors at risk for pulmonary fibrosis? *Am J Physiol Lung Cell Mol Physiol* 2021;320:L257–L265.
4. Libório-Ramos S, Barbosa-Matos C, Fernandes R, Borges-Pereira C, Costa S. Interstitial macrophages lead early stages of bleomycin-induced lung fibrosis and induce fibroblasts activation. *Cells* 2023;12:402.
5. Schiller HB, Montoro DT, Simon LM, Rawlins EL, Meyer KB, Strunz M, *et al.* The Human Lung Cell Atlas: a high-resolution reference map of the human lung in health and disease. *Am J Respir Cell Mol Biol* 2019;61: 31–41.
6. Adams TS, Schupp JC, Poli S, Ayaub EA, Neumark N, Ahangari F, *et al.* Single-cell RNA-seq reveals ectopic and aberrant lung-resident cell populations in idiopathic pulmonary fibrosis. *Sci Adv* 2020;6: eaba1983.
7. Deng CC, Hu YF, Zhu DH, Cheng Q, Gu JJ, Feng QL, *et al.* Single-cell RNA-seq reveals fibroblast heterogeneity and increased mesenchymal fibroblasts in human fibrotic skin diseases. *Nat Commun* 2021;12:3709.
8. Morse C, Tabib T, Sembrat J, Buschur KL, Bittar HT, Valenzi E, *et al.* Proliferating SPP1/MERTK-expressing macrophages in idiopathic pulmonary fibrosis. *Eur Respir J* 2019;54:1802441.
9. Reyfman PA, Walter JM, Joshi N, Anekalla KR, McQuattie-Pimentel AC, Chiu S, *et al.* Single-cell transcriptomic analysis of human lung provides insights into the pathobiology of pulmonary fibrosis. *Am J Respir Crit Care Med* 2019;199:1517–1536.

10. Travaglini KJ, Nabhan AN, Penland L, Sinha R, Gillich A, Sit RV, *et al.* A molecular cell atlas of the human lung from single-cell RNA sequencing. *Nature* 2020;587:619–625.
11. Jin S, Guerrero-Juarez CF, Zhang L, Chang I, Ramos R, Kuan C-H, *et al.* Inference and analysis of cell-cell communication using CellChat. *Nat Commun* 2021;12:1088.
12. Van de Sande B, Flerin C, Davie K, De Waegeneer M, Hulselmans G, Aibar S, *et al.* A scalable SCENIC workflow for single-cell gene regulatory network analysis. *Nat Protoc* 2020;15:2247–2276.
13. Iacono G, Massoni-Badosa R, Heyn H. Single-cell transcriptomics unveils gene regulatory network plasticity. *Genome Biol* 2019;20:110.
14. Yu G, Tzouvelekis A, Wang R, Herazo-Maya JD, Ibarra GH, Srivastava A, *et al.* Thyroid hormone inhibits lung fibrosis in mice by improving epithelial mitochondrial function. *Nat Med* 2018;24: 39–49.
15. Li Z, Yang J, Yan P, Pan X, Yuan H, Zhao M, *et al.* Thyroid hormone signal attenuates pulmonary fibrosis through cell interaction and communication in bleomycin-induced mouse lung [abstract]. *Am J Respir Crit Care Med* 2022;205:A1963.
16. Hao Y, Hao S, Andersen-Nissen E, Mauck WM III, Zheng S, Butler A, *et al.* Integrated analysis of multimodal single-cell data. *Cell* 2021;184: 3573–3587.e29.
17. Trapnell C, Cacchiarelli D, Grimsby J, Pokharel P, Li S, Morse M, *et al.* The dynamics and regulators of cell fate decisions are revealed by pseudotemporal ordering of single cells. *Nat Biotechnol* 2014;32: 381–386.
18. La Manno G, Soldatov R, Zeisel A, Braun E, Hochgerner H, Petukhov V, *et al.* RNA velocity of single cells. *Nature* 2018;560:494–498.
19. Shannon P, Markiel A, Ozier O, Baliga NS, Wang JT, Ramage D, *et al.* Cytoscape: a software environment for integrated models of biomolecular interaction networks. *Genome Res* 2003;13:2498–2504.
20. Feng J, Ding C, Qiu N, Ni X, Zhan D, Liu W, *et al.* Firmiana: towards a one-stop proteomic cloud platform for data processing and analysis. *Nat Biotechnol* 2017;35:409–412.
21. Dobin A, Davis CA, Schlesinger F, Drenkow J, Zaleski C, Jha S, *et al.* STAR: ultrafast universal RNA-seq aligner. *Bioinformatics* 2013;29: 15–21.
22. Heng TS, Painter MW; Immunological Genome Project Consortium. The Immunological Genome Project: networks of gene expression in immune cells. *Nat Immunol* 2008;9:1091–1094.
23. Jiang P, Gil de Rubio R, Hrycaj SM, Gurczynski SJ, Riemondy KA, Moore BB, *et al.* Ineffectual type 2-to-type 1 alveolar epithelial cell differentiation in idiopathic pulmonary fibrosis: persistence of the KRT8^{hi} transitional state. *Am J Respir Crit Care Med* 2020;201: 1443–1447.
24. Misharin AV, Morales-Nebreda L, Reyfman PA, Cuda CM, Walter JM, McQuattie-Pimentel AC, *et al.* Monocyte-derived alveolar macrophages drive lung fibrosis and persist in the lung over the life span. *J Exp Med* 2017;214:2387–2404.
25. Farbehi N, Patrick R, Dorison A, Xaymardan M, Janbandhu V, Wystub-Lis K, *et al.* Single-cell expression profiling reveals dynamic flux of cardiac stromal, vascular and immune cells in health and injury. *eLife* 2019;8:e43882.
26. Zhao W, Wang L, Wang Y, Yuan H, Zhao M, Lian H, *et al.* Injured endothelial cell: a risk factor for pulmonary fibrosis. *Int J Mol Sci* 2023; 24:8749.
27. Satoh T, Nakagawa K, Sugihara F, Kuwahara R, Ashihara M, Yamane F, *et al.* Identification of an atypical monocyte and committed progenitor involved in fibrosis. *Nature* 2017;541:96–101.
28. Aran D, Looney AP, Liu L, Wu E, Fong V, Hsu A, *et al.* Reference-based analysis of lung single-cell sequencing reveals a transitional profibrotic macrophage. *Nat Immunol* 2019;20:163–172.
29. Gibbings SL, Thomas SM, Atif SM, McCubbrey AL, Desch AN, Danhorn T, *et al.* Three unique interstitial macrophages in the murine lung at steady state. *Am J Respir Cell Mol Biol* 2017;57:66–76.
30. Henderson NC, Rieder F, Wynn TA. Fibrosis: from mechanisms to medicines. *Nature* 2020;587:555–566.
31. Plikus MV, Wang X, Sinha S, Forte E, Thompson SM, Herzog EL, *et al.* Fibroblasts: origins, definitions, and functions in health and disease. *Cell* 2021;184:3852–3872.
32. Peyser R, MacDonnell S, Gao Y, Cheng L, Kim Y, Kaplan T, *et al.* Defining the activated fibroblast population in lung fibrosis using single-cell sequencing. *Am J Respir Cell Mol Biol* 2019;61:74–85.
33. Ortiz-Zapater E, Signes-Costa J, Montero P, Roger I. Lung fibrosis and fibrosis in the lungs: is it all about myofibroblasts? *Biomedicines* 2022; 10:1423.
34. Yu G, Ibarra GH, Kaminski N. Fibrosis: lessons from OMICS analyses of the human lung. *Matrix Biol* 2018;68-69:422–434.
35. Neumark N, Cosme C Jr, Rose KA, Kaminski N. The idiopathic pulmonary fibrosis cell atlas. *Am J Physiol Lung Cell Mol Physiol* 2020; 319:L887–L893.
36. Mascharak S, desJardins-Park HE, Davitt MF, Griffin M, Borrelli MR, Moore AL, *et al.* Preventing *Engrailed-1* activation in fibroblasts yields wound regeneration without scarring. *Science* 2021;372:eaba2374.
37. Mora AL, Rojas M, Pardo A, Selman M. Emerging therapies for idiopathic pulmonary fibrosis, a progressive age-related disease. *Nat Rev Drug Discov* 2017;16:810.
38. Aspal M, Zemans RL. Mechanisms of ATII-to-ATI cell differentiation during lung regeneration. *Int J Mol Sci* 2020;21:3188.
39. Gao R, Peng X, Perry C, Sun H, Ntokou A, Ryu C, *et al.* Macrophage-derived netrin-1 drives adrenergic nerve-associated lung fibrosis. *J Clin Invest* 2021;131:e136542.
40. Maus UA, Janzen S, Wall G, Srivastava M, Blackwell TS, Christman JW, *et al.* Resident alveolar macrophages are replaced by recruited monocytes in response to endotoxin-induced lung inflammation. *Am J Respir Cell Mol Biol* 2006;35:227–235.
41. Byrne AJ, Maher TM, Lloyd CM. Pulmonary macrophages: a new therapeutic pathway in fibrosing lung disease? *Trends Mol Med* 2016; 22:303–316.
42. Espindola MS, Habiel DM, Narayanan R, Jones I, Coelho AL, Murray LA, *et al.* Targeting of TAM receptors ameliorates fibrotic mechanisms in idiopathic pulmonary fibrosis. *Am J Respir Crit Care Med* 2018;197: 1443–1456.
43. Bellan M, Cittone MG, Tonello S, Rigamonti C, Castello LM, Gavelli F, *et al.* Gas6/TAM system: a key modulator of the interplay between inflammation and fibrosis. *Int J Mol Sci* 2019;20:5070.
44. Urawa M, Kobayashi T, D'Alessandro-Gabazza CN, Fujimoto H, Toda M, Roeen Z, *et al.* Protein S is protective in pulmonary fibrosis. *J Thromb Haemost* 2016;14:1588–1599.
45. Fujino N, Kubo H, Maciewicz RA. Phenotypic screening identifies Axl kinase as a negative regulator of an alveolar epithelial cell phenotype. *Lab Invest* 2017;97:1047–1062.